The Astrophysical Journal, 618:413–425, 2005 January 1

IMPLICATIONS OF THE MEASURED IMAGE SIZE FOR THE RADIO AFTERGLOW OF GRB 030329

Jonathan Granot,[1] Enrico Ramirez-Ruiz,[1,2] and Abraham Loeb[3]

Received 2004 July 8; accepted 2004 September 7

ABSTRACT

We use data on the image size of the radio afterglow of GRB 030329 to constrain the physical parameters of this explosion. Together with the observed broadband spectrum, this data overconstrains the physical parameters, thus enabling us to test different GRB jet models for consistency. We consider two extreme models for the lateral spreading of the jet: model 1, with relativistic expansion in the local rest frame, and model 2, with little lateral expansion as long as the jet is highly relativistic. We find that both models are consistent with the data for a uniform external medium, while for a stellar wind environment model 1 is consistent with the data but model 2 is disfavored by the data. Our derivations can be used to place tighter constraints on the dynamics and structure of GRB jets in future afterglows, following a denser monitoring campaign for the temporal evolution of their image size.

Subject headings: gamma rays: bursts — ISM: jets and outflows — polarization — radiation mechanisms: nonthermal — relativity — shock waves

Online material: color figures

1. INTRODUCTION

It has long been recognized that direct imaging of gamma-ray bursts (GRBs) can provide important constraints on their physical parameters (Waxman 1997; Sari 1998; Panaitescu & Mészáros 1998; Granot et al. 1999a, 1999b; Granot & Loeb 2001). Unfortunately, the characteristic size of a GRB image is only of order 1 μas about a day after the GRB at the Hubble distance, and so it cannot be resolved by existing telescopes. Nevertheless, indirect constraints on the image size of GRB afterglows were derived based on the transition between diffractive and refractive scintillations (Goodman 1997) in the radio afterglow of GRB 970508 (Frail et al. 1997; Waxman et al. 1998), and based on microlensing by a star in a foreground galaxy (Loeb & Perna 1998) for the optical light curve of GRB 000301C (Garnavich et al. 2000; Granot & Loeb 2001; Gaudi & Loeb 2001; Mao & Loeb 2001; Gaudi et al. 2001).

Obviously, the challenge of imaging a GRB is made easier for nearby sources, where the late radio afterglow extends over a wide, possibly resolvable angle (Woods & Loeb 1999; Cen 1999; Wang & Loeb 2001; Paczyński 2001; Granot & Loeb 2003). Recently, Taylor et al. (2004) have used a VLBI campaign to measure, for the first time, the angular size and proper motion of the radio afterglow image of the bright, nearby ($z = 0.1685$) GRB 030329. The diameter of the afterglow image was observed to be $\sim$0.07 mas (0.2 pc) after 25 days and 0.17 mas (0.5 pc) after 83 days, indicating an average velocity of $\sim 4.1c$–$5.7c$. This superluminal expansion is consistent with expectations of the standard relativistic jet model (Oren et al. 2004). The projected proper motion of GRB 030329 was measured to be smaller than 0.3 mas for 80 days following the GRB.

Here we use the data of Taylor et al. (2004) to constrain the physical parameters of GRB 030329 based on detailed modeling of the collimated relativistic hydrodynamics of GRB afterglows. Since the current state-of-the-art modeling of afterglow jets is still flawed with uncertainties (Rhoads 1999; Sari et al. 1999; Granot et al. 2001; Kumar & Granot 2003; Salmonson 2003; Cannizzo et al. 2004), we use this data to critically assess some classes of models that were proposed in the literature. An important difference between relativistic radio jets of GRBs and the better studied relativistic radio jets of quasars (Begelman et al. 1984) or microquasars (Mirabel & Rodríguez 1999) is that active quasars often inject energy over extended periods of time into the jet while GRB sources are impulsive. Although quasar jets remain highly collimated throughout their lifetimes, GRB jets decelerate and expand significantly once they become nonrelativistic, $\sim$1 yr after the explosion. The hydrodynamic remnant of a GRB eventually becomes nearly spherical only after $\sim 5 \times 10^3$ yr (Ayal & Piran 2001).

The outline of the paper is as follows. In § 2 we discuss the expected image size of radio afterglows and its relation to the observed flux density below the self-absorption frequency. In § 3 we analyze the expected temporal evolution of the afterglow image size. The expected linear polarization is discussed in § 4, while the surface brightness profile across the image and its effects on the estimated source size are considered in § 5. Finally, we apply these derivations to the radio data of GRB 030329 (§ 6) and infer the physical parameters from the measured spectrum (§ 7). We conclude in § 8 with a discussion of our primary results and their implications.

2. THE IMAGE SIZE AND SYNCHROTRON SELF-ABSORPTION

In GRB afterglows, relativistic electrons are accelerated in the advancing shock wave to a power-law distribution of energies, $dN/d\gamma_e \propto \gamma_e^{-p}$ for $\gamma_e \geq \gamma_m$. For $p > 2$, the minimal Lorentz factor of the electrons is given by

$$\gamma_m = \left(\frac{p-2}{p-1}\right)\frac{m_p}{m_e}\epsilon_e(\Gamma - 1), \tag{1}$$

where ϵ_e is the fraction of the internal energy behind the shock in relativistic electrons and Γ is the bulk Lorentz factor of the shocked fluid. There is a spectral break at $\nu_m = \nu_{\rm syn}(\gamma_m)$, the synchrotron frequency of electrons with $\gamma_e = \gamma_m$. Another

[1] Institute for Advanced Study, Einstein Drive, Princeton, NJ 08540.
[2] Chandra Fellow.
[3] Harvard-Smithsonian Center for Astrophysics, 60 Garden Street, Cambridge, MA 02138.

break in the spectrum occurs at $\nu_c = \nu_{\rm syn}(\gamma_c)$, the synchrotron frequency of an electron that cools on the dynamical time.

At sufficiently low frequencies, below the self-absorption frequency $\nu_{\rm sa}$, the optical depth to synchrotron self-absorption τ_ν becomes larger than unity, causing an additional break in the spectrum. In this spectral range, the emitted intensity is given by the Rayleigh-Jeans part of a blackbody spectrum, where the blackbody temperature is taken as the effective temperature $T_{\rm eff}$ of the electrons that are emitting the radiation at the observed frequency ν. In the local rest frame of the emitting fluid this may be written as

$$I'_{\nu'} = \frac{2(\nu')^2}{c^2} k_{\rm B} T_{\rm eff} = \frac{2(\nu')^2}{c^2} \gamma_{\rm eff} m_e c^2, \tag{2}$$

where primed quantities are measured in the local rest frame of the emitting fluid, while unprimed quantities are measured in the observer frame (the rest frame of the central source). When $\nu_{\rm sa} > \nu_m$, the emission at $\nu_m < \nu < \nu_{\rm sa}$ is dominated by electrons for which $\nu \sim \nu_{\rm syn}(\gamma_e) \propto \gamma_e^2$, giving $\gamma_{\rm eff} \propto \nu^{1/2}$ and $F_\nu \propto I_\nu \propto \nu^{5/2}$. For $\nu_m > \nu_c$ there is fast cooling and all the electrons cool significantly within a dynamical time (Sari et al. 1998). When $\nu_m > \max(\nu_c, \nu_{\rm sa})$, then as ν decreases below $\nu_{\rm sa}$ the distance l behind the shock where $\tau_\nu(l) = 1$ decreases. The electrons in that location, which are responsible for most of the observed emission, have had less time to cool after passing the shock and therefore have a higher $T_{\rm eff} = \gamma_{\rm eff}(m_e c^2/k_{\rm B})$. In this case $\gamma_{\rm eff} \propto 1/l \propto \nu^{-5/8}$ and $F_\nu \propto \nu^{11/8}$ (Granot et al. 2000). At a sufficiently small distance behind the shock, smaller than l_c, an electron with an initial Lorentz factor γ_m does not have enough time to cool significantly after crossing the shock. Therefore, most electrons within a distance of l_c from the shock have $\gamma_e \sim \gamma_m$, and the effective temperature in this region is $T_{\rm eff} \approx \gamma_m m_e c^2/k_{\rm B}$. At sufficiently low frequencies (below $\nu_{\rm ac}$; see Granot et al. 2000), l becomes smaller than l_c and $\gamma_{\rm eff} \approx \gamma_m$ independent of ν, and therefore $F_\nu \propto \nu^2$ at $\nu < \nu_{\rm ac}$. For slow cooling ($\nu_m < \nu_c$), $\gamma_{\rm eff} \approx \gamma_m$ and $F_\nu \propto \nu^2$ immediately below $\nu_{\rm sa}$.

The observed specific intensity is given by $I_\nu = (\nu/\nu')^3 I'_{\nu'}$ and $\nu'/\nu = (1+z)\Gamma(1-\beta\cos\theta) \sim (1+z)/\Gamma$, where z is the source redshift and θ is the angle between the direction to the observer and the velocity vector of the emitting material in the observer frame. The observed flux density is $F_\nu = \int d\Omega \cos\tilde{\theta} I_\nu \approx \Omega I_\nu$, where $\Omega \approx \pi(R_\perp/D_A)^2 = (1+z)^2\pi(R_\perp/D_p)^2 = (1+z)^4\pi(R_\perp/D_L)^2$ and $\tilde{\theta} \cong \tan\tilde{\theta} = R_\perp/D_A \ll 1$ are the solid angle and angular radius of the source image, respectively. Here $R_\perp$ is the radius of the observed image (its apparent size on the plane of the sky) and D_A, D_p, and D_L are the angular, proper, and luminosity distances to the source, respectively. Thus one obtains $I_\nu \approx [\Gamma/(1+z)]^3[2(\nu')^2/c^2]kT_{\rm eff} \approx [\Gamma/(1+z)]2\nu^2\gamma_{\rm eff}m_e$ and (Katz & Piran 1997)

$$F_\nu \approx 2\pi\nu^2 m_e \Gamma \gamma_{\rm eff}(1+z)\left(\frac{R_\perp}{D_p}\right)^2. \tag{3}$$

In deriving equation (3) the specific intensity I_ν was assumed to be uniform across the observed image. A more accurate calculation would have to integrate over the contribution to the observed emission from different radii R and angles θ from the line of sight for a fixed observed time t (e.g., Granot et al. 1999b), which results in a nonuniform I_ν across the image. Therefore, when using equation (3) one must choose some effective value for I_ν that should correspond to its average value across the image. Since I_ν depends on Γ, this is equivalent to choosing an effective value of Γ. Since Γ depends on R, one also has to find at which R or θ should the value of Γ be evaluated in equations (1) and (3). Usually $\nu_{\rm sa} < \nu_m < \nu_c$, in which case $\gamma_{\rm eff} \approx \gamma_m$, so that I_ν depends on Γ not only through the Lorentz transformations but also through the value of γ_m; i.e., Γ enters into both equations (1) and (3). Comparing equation (3) with the more accurate expression calculated by Granot & Sari (2002) using the Blandford-McKee (1976) self-similar spherical solution, we find that the two expressions are in relatively good agreement[4] if Γ is evaluated just behind the shock at the location where $R_\perp$ is located. This should be a good approximation before the jet break time in the light curve,

$$t_j = \frac{(1+z)}{4c}\left[\frac{(3-k)E}{2\pi A c^2}\right]^{1/(3-k)}\theta_0^2 \approx \begin{cases} 0.66(1+z)(E_{51}/n_0)^{1/3}(\theta_0/0.1)^2 \text{ days} & k=0, \\ 0.34(1+z)(E_{51}/A_*)(\theta_0/0.1)^2 \text{ days} & k=2. \end{cases} \tag{4}$$

At $t > t_j$, however, it is less clear how well this approximation holds, and it might be necessary to evaluate Γ at a different location. In particular, as we shall see below, this approximation does not work well for model 2 with $k = 0$, where Γ needs to be evaluated near the head of the jet, rather than at the side of the jet where $R_\perp$ is located.

The image size is given by $R_\perp = \max(R\sin\theta)$ along the equal arrival time surface (see Fig. 1). The equal arrival time surface is the surface from where photons that are emitted at the shock front arrive to the observer simultaneously. Since the emission originates only from behind the shock front, the projection of the equal arrival time surface onto the plane of the sky (i.e., the plane perpendicular to the line of sight) determines the boundaries of the observed image and its apparent size (see Fig. 1). For a spherical shock front with any $R(t_{\rm lab})$, $R_\perp = \max(R\sin\theta)$ is located at an angle θ_* that satisfies $\cos\theta_* = \beta_*$ (see Appendix A), where β_* and $\Gamma_* = (1-\beta_*^2)^{-1/2}$ are the velocity (in units of c) and the Lorentz factor of the shock front[5] at θ_*. This implies that $R_\perp(t) = R_*(t)/\Gamma_*(t)$, where $R_*(t) = R(t,\ \cos\theta = \beta_*)$ is the radius of the shock at $\theta_* = \arccos\beta_*$. Therefore $\Gamma_* = \Gamma_{\rm sh}(R_*)$ and $\beta_* = \beta_{\rm sh}(R_*)$. Although the shock front is probably not simply a section of a sphere (Granot et al. 2001), we consider this a reasonable approximation for our purpose. The expression for θ_* in the more general case of an axially symmetric shock is given in Appendix A.

The apparent speed, $\beta_{\rm ap} = [(1+z)/c](dR_\perp/dt)$, has a simple form for a point source moving at an angle θ from our line of sight, $\beta_{\rm ap} = \beta_{\rm sh}\sin\theta/(1-\beta_{\rm sh}\cos\theta)$. Substituting $\cos\theta = \beta_{\rm sh}$ in this expression gives $\beta_{\rm ap} = \Gamma_*\beta_* = (\Gamma_*^2 - 1)^{1/2}$, or $\Gamma_* = (1+\beta_{\rm ap}^2)^{1/2}$ and $\beta_* = \beta_{\rm ap}/(1+\beta_{\rm ap}^2)^{1/2}$. In Appendix B we show that this result holds for any spherically symmetric shock front, and we also generalize it to an axially symmetric shock. Finally, the Lorentz factor Γ of the shocked fluid just behind the shock at θ_* is related to the Lorentz factor of the shock itself, Γ_*, by $\Gamma_*^2 = (\Gamma+1)[\hat{\gamma}(\Gamma-1)+1]^2/[\hat{\gamma}(2-\hat{\gamma})(\Gamma-1)+2]$ (Blandford

[4] We find that the ratio of the numerical coefficient in eq. (3) to that in Granot & Sari (2002) is in this case $1.09(3p-1)/(3p+2)$ for $k=2$ and $1.71(3p-1)/(3p+2)$ for $k=0$.

[5] Note that we use $\beta_{\rm sh}$ or $\Gamma_{\rm sh}$ for the location of the emitting fluid, which is always just behind the shock. On the other hand, we use β or Γ (which are slightly smaller than $\beta_{\rm sh}$ or $\Gamma_{\rm sh}$, respectively) for the Lorentz transformations of the emitted radiation, since these are the bulk velocity and Lorentz factor of the emitting fluid.

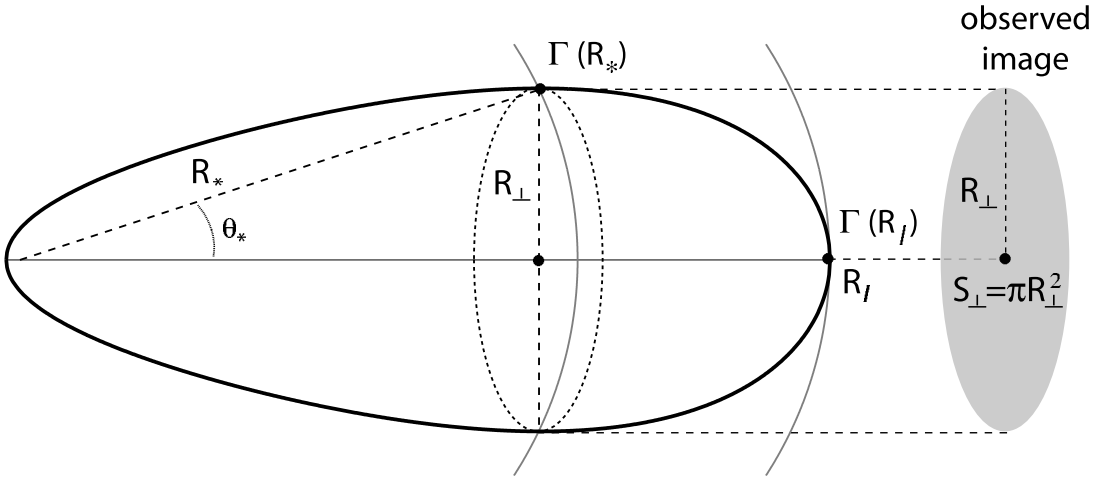

FIG. 1.—Schematic illustration of the equal arrival time surface (*thick black line*), namely, the surface from where the photons emitted by the shock front arrive at the same time to the observer (on the far right-hand side). The maximal lateral extent of the observed image, $R_\perp$, is located at an angle θ_*, where the shock radius and Lorentz factor are R_* and $\Gamma_* = \Gamma_{\rm sh}(R_*)$, respectively. The area of the image on the plane of the sky is $S_\perp = \pi R_\perp^2$. The shock Lorentz factor $\Gamma_{\rm sh}$ varies with R and θ along the equal arrival time surface. The maximal radius R_l on the equal arrival time surface is located along the line of sight. If, as expected, $\Gamma_{\rm sh}$ decreases with R, then $\Gamma_l = \Gamma_{\rm sh}(R_l)$ is the minimal shock Lorentz factor on the equal arrival time surface.

& McKee 1976), where $\hat{\gamma}$ is the adiabatic index of the shocked fluid. For $\Gamma_* \gg 1$, $\hat{\gamma} = 4/3$ and $\Gamma = \Gamma_*/\sqrt{2}$.

3. THE TEMPORAL EVOLUTION OF THE IMAGE SIZE

For simplicity, we consider a uniform GRB jet with sharp edges and a half-opening angle θ_j, with an initial value of θ_0. The evolution of the angular size of the image and its angular displacement from the central source on the plane of the sky, for viewing angles $\theta_{\rm obs} > \theta_0$ from the jet axis, was outlined in Granot & Loeb (2003). Here we expand this discussion to include viewing angles within the initial jet opening angle, $\theta_{\rm obs} < \theta_0$, for which there is a detectable prompt gamma-ray emission (similarly to GRB 030329, which is considered in the next section). For $\theta_{\rm obs} < \theta_0$, $R_\perp$ is the observed size of the image, while for $\theta_{\rm obs} > \theta_0$ it represents the displacement with respect to the central source on the plane of the sky.

In this section we concentrate on a viewing angle along the jet axis, $\theta_{\rm obs} = 0$, and in the next section we briefly outline the expected differences for $0 < \theta_{\rm obs} < \theta_0$. For $\theta_{\rm obs} = 0$, the observed image is symmetric around the line of sight (to the extent that the jet is axisymmetric). At $t < t_j$ the edge of the jet is not visible and the observed image is the same as for a spherical flow: $R_\perp \propto (E_{\rm iso}/A)^{1/2(4-k)} t^{(5-k)/2(4-k)} \propto (E/A)^{1/2(3-k)} t_j^{-1/2(4-k)} t^{(5-k)/2(4-k)}$ for an external density profile $\rho_{\rm ext} = Ar^{-k}$, i.e., $a = (5-k)/2(4-k)$, where $a \equiv d \ln R_\perp / d \ln t$. Here E is the true kinetic energy of the jet and $E_{\rm iso} = f_b^{-1} E$ is the isotropic equivalent energy, where $f_b = 1 - \cos\theta_0 \approx \theta_0^2/2$ is the beaming factor. At $t < t_j$ the flow is described by the Blandford-McKee (1976) self-similar solution, which provides an accurate expression for the image size (Granot et al. 1999a; Granot & Sari 2002),

$$R_\perp = \left[\frac{2^{2-k}(17-4k)(4-k)^{5-k} E_{\rm iso} c^{3-k} t^{5-k}}{\pi (5-k)^{5-k} (1+z)^{5-k} A}\right]^{1/2(4-k)} = \begin{cases} 3.91 \times 10^{16} (E_{\rm iso,\,52}/n_0)^{1/8} [t_{\rm days}/(1+z)]^{5/8} \ {\rm cm} & k = 0, \\ 2.39 \times 10^{16} (E_{\rm iso,\,52}/A_*)^{1/4} [t_{\rm days}/(1+z)]^{3/4} \ {\rm cm} & k = 2. \end{cases} \quad (5)$$

At $t > t_{\rm NR}$ the jet gradually approaches the Sedov-Taylor self-similar solution, asymptotically reaching $R_\perp \propto (Et^2/A)^{1/(5-k)}$, i.e., $a = 2/(5-k)$. At $t_j < t < t_{\rm NR}$ there is a large uncertainty in the hydrodynamic evolution of the jet, and in particular in its rate of sideways expansion. We therefore consider two extreme assumptions that should roughly bracket the different possible evolutions of $R_\perp(t)$: (1) relativistic lateral expansion in the comoving frame (Rhoads 1999; Sari et al. 1999), for which $\theta_j \approx \max(\theta_0, \gamma^{-1})$ so that at $t_j < t < t_{\rm NR}$ we have $\gamma \approx \theta_j^{-1} \approx \theta_0^{-1} \exp(-R/R_j)$, and (2) little or no lateral expansion, $\theta_j \approx \theta_0$ for $t < t_{\rm NR}$, in which case appreciable lateral expansion occurs only when the jet becomes subrelativistic and gradually approaches spherical symmetry. We refer to these models as model 1 and model 2, respectively. Model 2 is also motivated by the results of numerical simulations (see Fig. 2) that show only modest lateral expansion as long as the jet is relativistic (Granot et al. 2001; Kumar & Granot 2003; Cannizzo et al. 2004). These numerical results are also supported by a simple analytic argument that relies on the shock jump conditions for oblique relativistic shocks (Kumar & Granot 2003).

Figure 3 schematically shows the evolution of $R_\perp(t)$ for these two extreme models, both when viewed on-axis ($\theta_{\rm obs} < \theta_0$), as required for seeing the prompt gamma-ray emission, and for $\theta_{\rm obs} \approx 90^\circ$, as will typically be the case for GRB jets found in nearby Type Ib/c supernovae (Paczyński 2001; Granot & Loeb 2003; Granot & Ramirez-Ruiz 2004; Ramirez-Ruiz & Madau 2004). For $\theta_{\rm obs} < \theta_0$ at $t_j < t < t_{\rm NR}$, we have $R_\perp \propto (E/A)^{1/2(3-k)} t^{1/2}$ for model 1 and $R_\perp \propto (E_{\rm iso} t/A)^{1/(4-k)} \propto (E/A)^{1/(3-k)} (t/t_j)^{1/(4-k)}$ for model 2. Therefore, with $k = 2$ we have $a = \frac{1}{2}$ for both models, despite their very different jet dynamics. For $k = 0$ we have $a = \frac{1}{2}$ for model 1 and $a = \frac{1}{4}$ for model 2.

In model 1, the jet is already relatively close to being spherical (i.e., $\theta_j \sim 1$) at $t_{\rm NR} = t_{\rm NR}(E)$, where $R_{\rm NR}(E) = ct_{\rm NR}(E) = [(3-k)E/4\pi A c^2]^{1/(3-k)}$, and its radius is similar to that of the Sedov-Taylor solution, $R_{\rm ST}(E,t) = \xi (Et^2/A)^{1/(5-k)}$, corresponding to the same time t, where $\xi = \xi(k, \hat{\gamma}) \sim 1$. Therefore, we expect it to approach spherical symmetry in a few dynamical times, i.e., when the radius increases by a factor of $b \sim$ a few, corresponding to a factor of $\sim b^{(5-k)/2}$ in time, and the transition between the asymptotic power laws in $R_\perp(t)$ is expected to be smooth and monotonic.

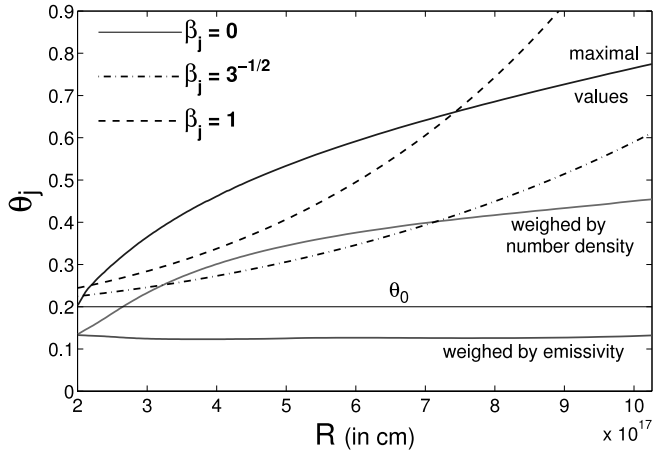

FIG. 2.—Evolution of the jet half-opening angle θ_j as a function of radius R for various illustrative cases. The solid line shows the evolution derived from two-dimensional hydrodynamic simulations (Granot et al. 2001). The different lines give the maximal polar angle θ of the shock front (which is obtained at a relatively small radius where a minor fraction of the emission is produced) and the average values of θ within the jet when averaged over the circumburst gas density and over the total emissivity. Most of the emission comes from within the original jet opening angle, $\theta_0 = 0.2$. Also shown is the evolution of $\theta_j(R)$ predicted by simple semianalytic models. Three illustrative cases are depicted in which the lateral expansion speed is assumed to be $\beta_j = 0$, $3^{-1/2}$, and 1 in the local rest frame (Rhoads 1999; Sari et al. 1999; Oren et al. 2004). Since the onset of lateral expansion in the simple models takes place at a somewhat larger radius (R_j), a higher value of gas density is adopted for these models in order to show more easily their different qualitative behaviors. [*See the electronic edition of the Journal for a color version of this figure.*]

In model 2, however, the jet becomes subrelativistic only at $R_{\rm NR}(E_{\rm iso}) = ct_{\rm NR}(E_{\rm iso})$, which is a factor of $\sim(E_{\rm iso}/E)^{1/(3-k)} = f_b^{-1/(3-k)} \sim \theta_0^{-2/(3-k)}$ larger than $R_{\rm NR}(E) = ct_{\rm NR}(E)$ and a factor of $\sim f_b^{-1/(5-k)} \sim \theta_0^{-2/(5-k)}$ larger than $R_{\rm ST}[E, t_{\rm NR}(E_{\rm iso})]$. It also keeps its original opening angle, $\theta_j \approx \theta_0$, until $t_{\rm NR}(E_{\rm iso})$, and hence at this time the jet is still very far from being spherical. Thus, once the jet becomes subrelativistic, we expect it to expand sideways significantly and to become roughly spherical only when it has increased its radius by a factor of $b \sim$ a few. This should occur, however, roughly at a time $t_{\rm sph}$ when $R_{\rm ST}(E, t_{\rm sph}) = bR_{\rm NR}(E_{\rm iso})$, i.e.,

$$t_{\rm sph}/t_{\rm NR}(E_{\rm iso}) \approx f_b^{-1/2} b^{(5-k)/2} \approx \sqrt{2}\theta_0^{-1} b^{(5-k)/2}. \quad (6)$$

This is a factor of $\sim f_b^{-1/2} \approx 14(\theta_0/0.1)^{-1}$ larger than the expected transition time in model 1, and for $b \sim 2$–3 gives a factor of $\sim(80$–$220)(\theta_0/0.1)^{-1}$ for $k = 0$ and $\sim(40$–$70)(\theta_0/0.1)^{-1}$ for $k = 2$. During this transition time, $R_\perp(\theta_{\rm obs} < \theta_0)$ grows by a factor of $\sim f_b^{-1/2} b \sim \theta_0^{-1} b$ while $R_\perp(\theta_{\rm obs} \approx 90^\circ)$ grows by a factor of $\sim b$. This implies that during the transition,

$$\langle a \rangle = \begin{cases} \dfrac{\ln b - (1/2)\ln f_b}{[(5-k)/2]\ln b - (1/2)\ln f_b} & \theta_{\rm obs} < \theta_0, \\ \dfrac{\ln b}{[(5-k)/2]\ln b - (1/2)\ln f_b} & \theta_{\rm obs} = 90^\circ, \end{cases} \quad (7)$$

and $0 < \langle a \rangle < 2/(5-k)$ for $\theta_{\rm obs} < \theta_0$ while $2/(5-k) < \langle a \rangle < 1$ for $\theta_{\rm obs} = 90^\circ$, where $\langle a \rangle \approx 2/(5-k)$ in the limit $b \gg \theta_0^{-1}$ (which is not very realistic). The other limiting value of $\langle a \rangle \approx 0$ for $\theta_{\rm obs} < \theta_0$ and $\langle a \rangle \approx 1$ for $\theta_{\rm obs} = 90^\circ$ is approached in the limit $b \ll \theta_0^{-1}$. Typical parameter values ($b \sim 2$–3, $\theta_0 \sim 0.05$–0.2) are somewhat closer to the latter limit. For example, for $k = 0$, $b = 2.5$, and $\theta_0 = 0.1$ we have $\langle a \rangle \approx 0.722$ for $\theta_{\rm obs} < \theta_0$ and $\langle a \rangle \approx 0.185$ for $\theta_{\rm obs} = 90^\circ$. This demonstrates that for on-axis observers there should be a sharp rise in $R_\perp$, while for observers at $\theta_{\rm obs} \approx 90^\circ$ there should be a very moderate rise in $R_\perp$ during the transition phase from the asymptotic $t_j \ll t \ll t_{\rm NR}$ and $t \gg t_{\rm NR}$ regimes. Furthermore, as is illustrated in Figure 3, this transition would not be monotonic in model 2. This is because during the transition a passes through values larger (smaller) than both of its asymptotic values for $\theta_{\rm obs} < \theta_0$ ($\theta_{\rm obs} \approx 90^\circ$).

For comparison, and in order to perform a quantitative comparison with the data, we consider a simple semianalytic model where the shock front at any given lab-frame time occupies a section of a sphere within $\theta < \theta_j$ and $R_\perp$ is located at $\theta_\perp = \min(\theta_*, \theta_j)$. The observer time assigned to a given $\theta_\perp(t_{\rm lab})$ is $t = t_{\rm lab} - [R(t_{\rm lab})/c]\cos\theta_\perp(t_{\rm lab})$. We follow Oren et al. (2004) with minor differences: (1) we choose the normalization of $R_\perp$ at $t \ll t_j$ so that it will coincide with the value given by the Blandford-McKee solution (i.e., eq. [5]), and (2) the lateral spreading velocity in the comoving frame, β_j, for model 2 smoothly varies from $\beta_j \ll 1$ at $t \ll t_{\rm NR}$ to the sound speed, $\beta_j \approx c_s/c$, at $t > t_{\rm NR}$. The latter is achieved by taking β_j to be the sound speed suppressed by some power of Γ.

Figure 4 shows the resulting $R_\perp(t)$ for ISM ($k = 0$) and stellar wind ($k = 2$) environments and different recipes for β_j. For a given β_j recipe, $R_\perp(t)$ depends on E/A and θ_0. The values of these parameters that were used in Figure 4 are indicated in the figure. For $k = 2$ the spread in $R_\perp(t)$ for the different β_j recipes is smaller than for $k = 0$. This is understandable since the asymptotic values of a are the same for models 1 and 2. There is still a nonnegligible spread, however, since the asymptotic value of $a = \frac{1}{2}$ at $t_j \ll t \ll t_{\rm NR}$ is not reached.[6] At $t \gg t_{\rm NR}$ all recipes for β_j approach the same value of $R_\perp(t)$, except for $\beta_j = 0$, for which $R_\perp(t)$ is smaller by a factor of $\sin\theta_0$. For $\beta_j = 0$ and $k = 0$ there is a pronounced flattening in $R_\perp(t)$ at $\sim$1.2 days, which is a factor of $\sim$7 larger than the value of $t_j = 0.165$ days that is implied by equation (4). We must stress that this simple model becomes unrealistic around $t_{\rm NR}$.

The apparent velocity of a point source is $\beta_{\rm ap} = \beta\sin\theta/(1 - \beta\cos\theta)$. For $\theta_{\rm obs} > \theta_0$, as long as $\theta_j < \theta_{\rm obs}$ and $t < t_{\rm NR}$ we have $\beta_{\rm ap} \approx 2\Gamma_{\rm sh}^2\theta/[1 + (\Gamma_{\rm sh}\theta)^2] \approx 2/\theta$. For $\theta_{\rm obs} = \pi/2$ we have $\beta_{\rm ap} = \beta_{\rm sh}$, which is close to 1 at $t < t_{\rm NR}$. For $\Gamma_{\rm sh} \gg 1$ and $\theta > \Gamma_{\rm sh}^{-1}$ we have $\beta_{\rm ap} \approx \sin\theta/(1 - \cos\theta)$, so that $\beta_{\rm ap} > 1$ for $\theta_{\rm obs} < \pi/2$ and $\beta_{\rm ap} < 1$ for $\theta_{\rm obs} > \pi/2$ (i.e., for the counter jet, assuming a double-sided jet; see Fig. 2 of Granot & Loeb 2003). For $\theta_{\rm obs} < \theta_0$ we have $\beta_{\rm ap} = \Gamma_*\beta_* \approx \Gamma_*$ at $t < t_{\rm NR}$. At $t < t_j$ we get $\theta_\perp = \theta_* < \theta_0$ and the shock front is roughly spherical with an approximately uniform Lorentz factor within $\theta \lesssim \theta_*$, so that $\Gamma_* \approx \Gamma_{\rm sh}$. At $t_j < t < t_{\rm NR}$ we have $\theta_* \approx \theta_j \approx \Gamma_{\rm sh}^{-1}$ and $\beta_{\rm ap} \approx \Gamma_* \approx \Gamma_{\rm sh}$ for model 1, suggesting that using $\Gamma(\theta_*)$ for calculating the emission (i.e., in eqs. [1], [3], and [8]) is a reasonable approximation. For model 2, $\theta_* \approx \theta_j \approx \theta_0$ and $\beta_{\rm ap} \approx \Gamma_* \approx 2\theta_0\Gamma_{\rm sh}^2$, so that[7] $\Gamma_*/\Gamma_{\rm sh} \approx 2\theta_0\Gamma_{\rm sh} < 1$, suggesting that $\Gamma(\theta_*)$ underestimates the effective value of the emissivity-weighted Γ, which enters the expressions for the observed emission. This results from the fact that in model 2 most of the emission at

[6] This is because it takes a long time to approach this limit for $k = 2$, which is longer than the dynamical range between t_j and $t_{\rm NR}$.

[7] Here $\Gamma_{\rm sh}$ represents the uniform-shock Lorentz factor in the simple semianalytic model described at the end of § 2, where the shock at any given $t_{\rm lab}$ occupies a section of a sphere and abruptly ends at θ_j, and at $t_j < t < t_{\rm NR}$ $R_\perp$ is located at θ_j. On the other hand, $\Gamma_* = \Gamma_{\rm sh}(\theta_*)$ is the Lorentz factor at the angle θ_* where $R_\perp$ is located for a smooth and continuous (and therefore more realistic) shock front, for which $\Gamma_{\rm sh}$ changes with θ at a given $t_{\rm lab}$.

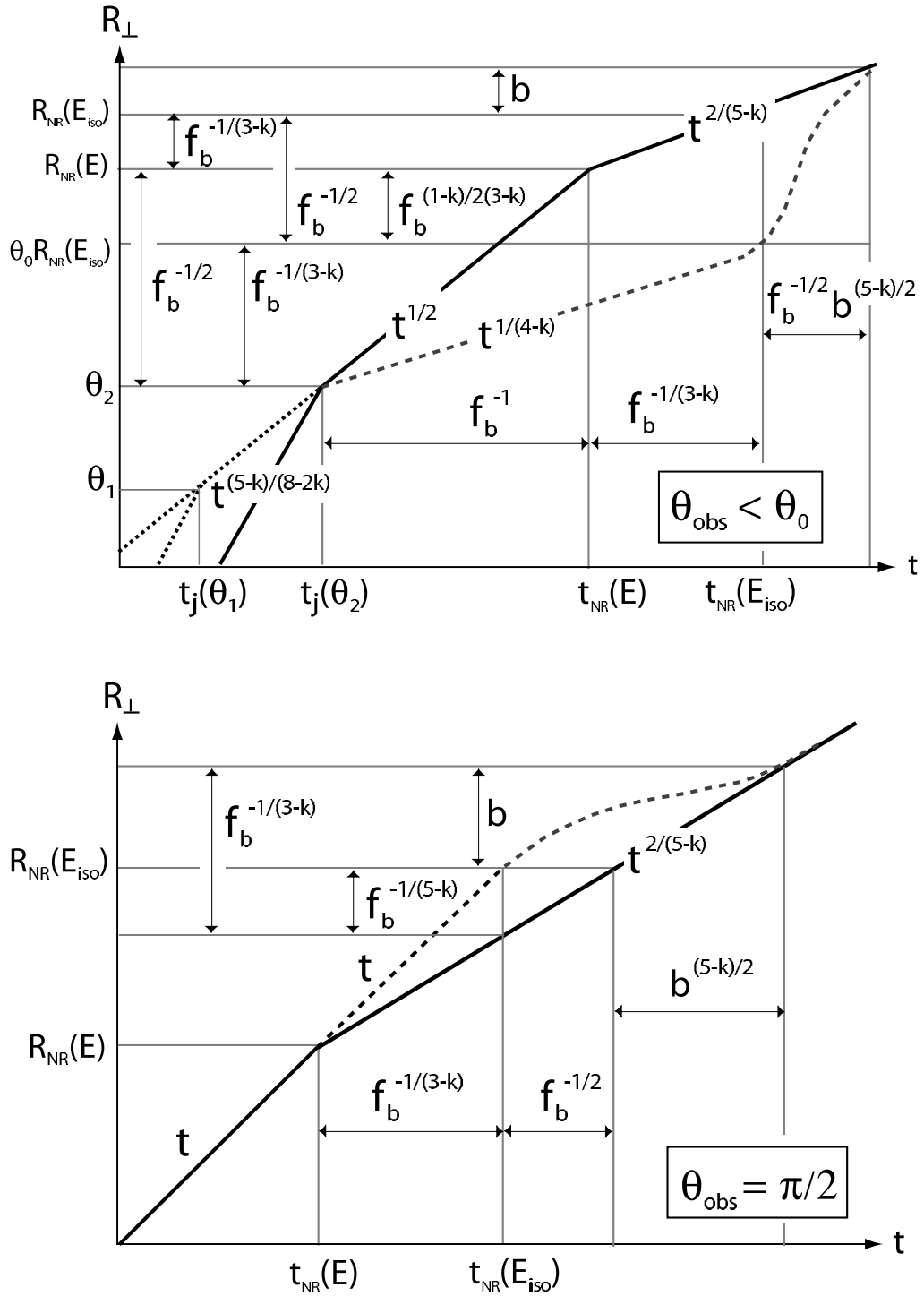

FIG. 3.—Schematic plot of the evolution of the observed afterglow image size $R_\perp$ of a uniform GRB jet with sharp edges. The jet is viewed either from within the initial jet opening angle, $\theta_{\rm obs} < \theta_0$ (*top*), or from $\theta_{\rm obs} \approx 90^\circ$ (*bottom*). The solid line is for model 1 (relativistic lateral expansion in the local rest frame), and the dashed line is for model 2 (little or no lateral expansion before $t_{\rm NR}$). The dotted line in the top panel represents jets (in model 2) with a smaller θ_0 and the same true energy E, which converge to the same self-similar dynamics and therefore the same $R_\perp(t)$ after the jet break time t_j. Also shown are the ratios of various values of $R_\perp$ and t.

$t_j < t < t_{\rm NR}$ originates from $\theta < \theta_0$, where Γ is higher than at $\theta_* \gtrsim \theta_0$ (see Fig. 2 and Granot et al. 2001).

4. LINEAR POLARIZATION

For $0 < \theta_{\rm obs} < \theta_0$ the image would not be symmetric around the line of sight, but its typical angular size would be similar to that for $\theta_{\rm obs} = 0$. If there is significant lateral spreading at $t > t_j$, then this should cause the image to become more symmetric around our line of sight with time. This, by itself, might be a possible diagnostic for the degree of lateral spreading. The degree of asymmetry in the observed image should also be reflected in the degree of linear polarization and its temporal evolution. While the image might be resolved only for a very small number of sufficiently nearby GRBs, the linear polarization might be measured for a larger fraction of GRBs.

Contrary to naive expectations, for very slow lateral expansion ($\beta_j \ll 1$) the polarization decays faster after its peak at $t \sim t_j$, compared to lateral expansion at the local sound speed,

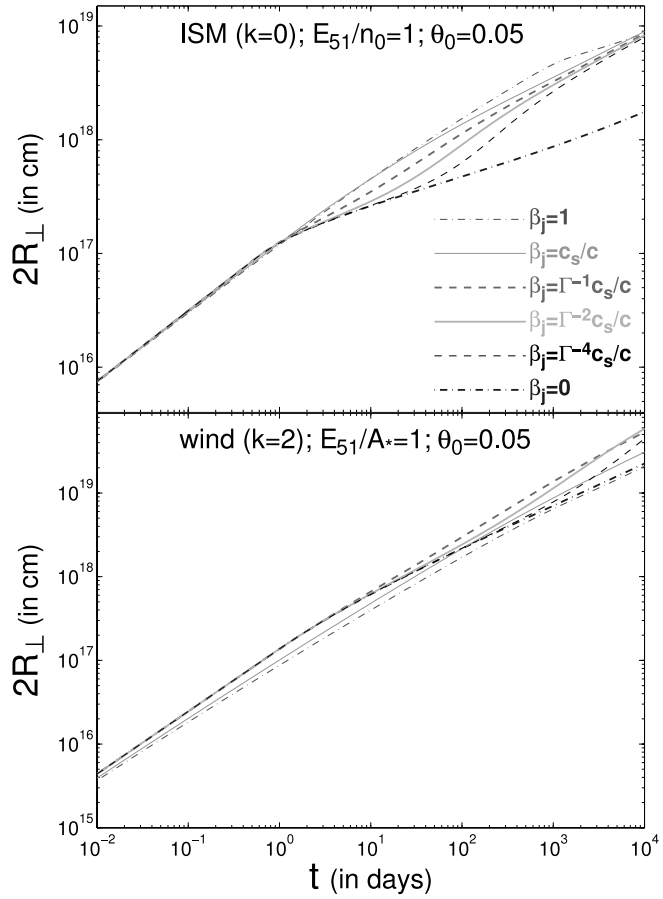

FIG. 4.—Evolution of the source size (or more precisely, its diameter $2R_\perp$) as a function of time, for a uniform density environment ($k = 0$; *top*) and for a stellar wind ($k = 2$; *bottom*). Different recipes are considered for the lateral spreading velocity in the comoving frame, β_j. See text for more details. [*See the electronic edition of the Journal for a color version of this figure.*]

$\beta_j = c_s/c \approx 3^{-1/2}$, in the comoving frame (Rossi et al. 2004). A very fast lateral expansion in the local frame close to the speed of light ($\beta_j \approx 1$) leads to $\theta_j \approx \max(\theta_0, \gamma^{-1})$ and to three peaks in the polarization light curve, where the polarization position angle changes by 90° as the degree of polarization passes through zero between the peaks (Sari 1999). When there is a slower lateral expansion or no lateral expansion at all (Ghisellini & Lazzati 1999), there are only two peaks in the polarization light curve, where again the polarization position angle changes by 90° as the degree of polarization passes through zero between the peaks. The peak polarization is higher for $\beta_j \approx 0$ (∼15%–16%), compared to $\beta_j = 3^{-1/2}$ (∼9%) (Rossi et al. 2004). The maximal observed degree of polarization is, however, usually $\lesssim$3%, suggesting that the magnetic field configuration behind the shock is more isotropic than a random field fully within the plane of the shock (Granot & Königl 2003), which is expected if the magnetic field is produced by the Weibel instability (Medvedev & Loeb 1999). This changes the overall normalization of the polarization light curve, and hardly affects its shape (Granot & Königl 2003). Since the overall normalization is the most pronounced difference between slow and fast lateral expansion, and since it is very similar to the effect of the degree of anisotropy of the magnetic field behind the shock, it would be very hard to constrain the degree of lateral expansion from the polarization light curves. There are also other possible complications, such as a small ordered magnetic field component (Granot & Königl 2003), which can induce polarization that is not related to the jet structure.

Taylor et al. (2004) put a 3 σ upper limit of 1% on the linear polarization in the radio ($\nu = 8.4$ GHz) at $t = 7.71$ days. They attribute the low polarization to synchrotron self-absorption. Indeed, $\nu_{\rm sa}$ is above 8.4 GHz at this time, but only by a factor of ∼2. One might expect a suppression of the polarization in the self-absorbed region of the synchrotron spectrum, since it should follow the Rayleigh-Jeans part of a blackbody spectrum and depend only on the electron distribution (i.e., the "effective temperature"), and not on the details of the magnetic field (Granot et al. 1999b). The optical depth to self-absorption does, however, depend on the details of the magnetic field and may thereby vary with the direction of polarization. Therefore, there might still be polarization at $\nu \lesssim \nu_{\rm sa}$, which will go to zero in the limit $\nu \ll \nu_{\rm sa}$. An ordered magnetic field in the shocked fluid through which the emitted synchrotron radiation propagates on its way to the observer might induce some polarization in the observed radiation (Sagiv et al. 2004). These effects are suppressed roughly by a factor of the square root of the ratio between the magnetic field coherence length and the width of the emitting region (which is of the order of the typical path length of an emitted photon through the shocked plasma before it escapes the system).

5. THE SURFACE BRIGHTNESS PROFILE

Taylor et al. (2004) use a circular Gaussian profile for their quoted values, and also tried a uniform disk and thin ring. They find that a Gaussian with an angular diameter size of 1 mas is equivalent to a uniform disk with an angular diameter of 1.6 mas and a thin ring with an angular diameter of 1.1 mas. At $t < t_j$ the jet dynamics are close to that of a spherical flow, since the center of the jet is not in causal contact with its edge, and the dynamics can be described by the Blandford-McKee (1976) spherical self-similar solution (within the jet, at $\theta < \theta_0$). The surface brightness in this case has been investigated at length in several works (Waxman 1997; Sari 1998; Panaitescu & Mészáros 1998; Granot et al. 1999a, 1999b; Granot & Loeb 2001). The surface brightness profile of the image, normalized by its average value across the image, is the same within each power-law segment of the spectrum, but changes between different power-law segments (Granot & Loeb 2001). The afterglow image is limb brightened, resembling a ring, in the optically thin part of the spectrum, and more uniform, resembling a disk, in the self-absorbed part of the spectrum. This can affect the angular size of the image that is inferred from the observations (Taylor et al. 2004), where the angular diameter for a uniform disk (thin ring) is a factor of 1.6 (1.1) larger than the values quoted by Taylor et al. (2004) for a circular Gaussian surface brightness profile. This effect would be more important at $\nu \lesssim \nu_{\rm sa}$, where the afterglow image resembles a uniform disk rather than a thin ring.

One should keep in mind that the image size of GRB 030329 was inferred well after the jet break time, $t \gg t_j$, and relatively close to the nonrelativistic transition time, $t \sim t_{\rm NR}$. However, at $t_j < t < t_{\rm NR}$ the jet dynamics is poorly known, and this uncertainty must necessarily be reflected in any calculation of the afterglow image at this stage, which could only be as good as the assumed dynamical model of the jet. The afterglow image at this stage was calculated by Ioka & Nakamura (2001) assuming lateral expansion at the local sound speed (Rhoads 1999), similar to our model 1. They find that at $t < t_j$ the surface brightness diverges at the outer edge of the image, which is an artifact of their assumption of emission from a two-dimensional

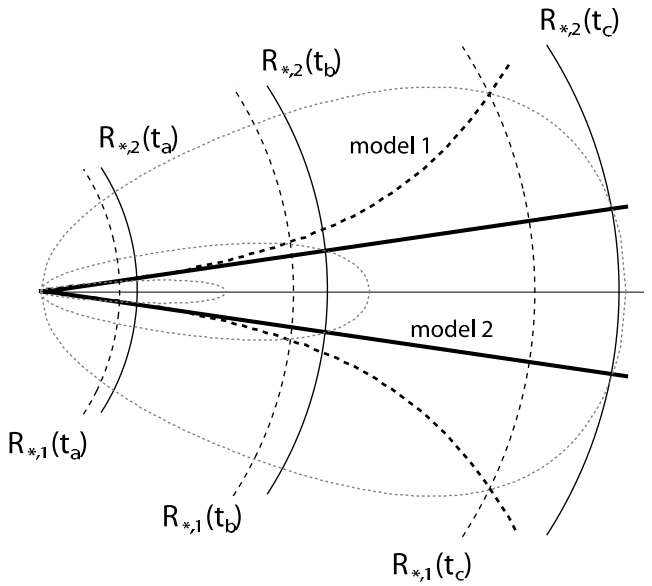

FIG. 5.—Evolution of the source size as a function of time for $t > t_j$. In model 1, the lateral expansion in the local frame is relativistic, while in model 2 there is no lateral expansion at $t > t_j$. The shock front at any given time $t_{\rm lab}$ is assumed to be part of a sphere that abruptly ends at a finite angle θ_j from the jet axis. The gray dotted lines represent the equal arrival time surfaces at three different observed times. Since the jet dynamics $R(t_{\rm lab})$ are different for models 1 and 2, the equal arrival time surfaces should be different (but in this sketch, for simplicity, we depict them as being equal). At $t > t_j$ [where $\theta_j(R_*) < \theta_*$], the edge of the image, which determines the image size, is located at the edge of the jet, i.e., at an angle θ_j instead of θ_*.

surface (Sari 1998; Granot & Loeb 2001) identified with the shock front. Calculating the contribution from all the volume of the emitting fluid behind the shock makes this divergence go away, except for certain power-law segments of the spectrum where the emission indeed arises from a very thin layer just behind the shock (Granot & Loeb 2001). At $t > t_j$ Ioka & Nakamura (2001) obtain a relatively uniform surface brightness profile. However, this is due to the unphysical assumption that the shock front at any given lab-frame time is part of a sphere within some finite angle θ_j from the jet symmetry axis where the jet ends abruptly. The edge of the image in this case corresponds to this unphysical point where the jet ends abruptly (see Fig. 5). More physically, as is shown by numerical simulations (Granot et al. 2001), the shock front is not a section of a sphere and is instead round without any sharp edges. Similarly to the spherical-like evolution at $t < t_j$, the edge of the image would in this case correspond to $R_\perp = \max(R\sin\theta)$, and thus the image is expected to be limb brightened for the same qualitative reasons that apply at $t < t_j$, even though there would be some quantitative differences. A proper calculation of the afterglow image at $t > t_j$ requires full numerical simulations of the jet dynamics.

6. APPLICATION TO GRB 030329

We now apply the expressions derived in the previous section to GRB 030329, which occurred at a redshift of $z = 0.1685$. We use the image angular diameter size of $\theta_s \approx 70$ μas for[8] $D_A \approx 587$ Mpc that was inferred at $t = 24.5$ days (Taylor et al. 2004), which corresponds to $R_\perp \approx 0.1$ pc. This implies an average apparent velocity of $\langle\beta_{\rm ap}\rangle = (1+z)R_\perp/ct \approx 5.66$. The instantaneous apparent velocity is given by $\beta_{\rm ap} \equiv [(1+z)/c]dR_\perp/dt = a\langle\beta_{\rm ap}\rangle$, where $a \equiv d\ln R_\perp/d\ln t$. For GRB 030329, if we also take into account the inferred source size of $\theta_s \approx 170$ μas or $R_\perp \approx 0.25$ pc at $t = 83.3$ days and the 2 σ upper limit of $\theta_s < 100$ μas or $R_\perp < 0.14$ pc at $t = 51.3$ days (Taylor et al. 2004), we have[9] $a = 0.71^{+0.4}_{-0.3}$ (1 σ). This value is between $t = 24.5$ and 83.3 days, assuming that $R_\perp(t)$ followed a perfect power-law behavior $\propto t^a$ with $a = $ const during this time. This is a reasonable approximation for model 1 or model 2 with $k = 2$, for which $a = \frac{1}{2}$ at $t_j < t < t_{\rm NR}$, and therefore these models are consistent with the observed temporal evolution of the image size. For model 1 with $k = 0$ (see § 3), $a = \frac{1}{4}$ at $t_j \ll t \ll t_{\rm NR}$, but its value is expected to increase significantly near $t_{\rm NR}$, which we find to be at $\sim$200 days for this model (see Table 1). Therefore, it can still account for the observed image size at $t = 24.5$ and 83.3 days, together with the upper limits at 51.3 days. At $t = 24.5$ days, however, we still expect the value of a in model 2 with $k = 0$ to be relatively close to its asymptotic value of $a = \frac{1}{4}$.

Figure 6 shows crude fits between the simple semianalytic realization of models 1 and 2 (which is described at the end of § 3) and the observed image size (Taylor et al. 2004). For model 2 we have used the recipe $\theta_j = \Gamma^{-1}(c_s/c)$ for the lateral expansion. We have treated the value of E/A as a free parameter whose value was varied in order to get a good fit, while the value of θ_0 was determined according to the observed jet break time $t_j \approx 0.5$ days using equation (4). In the latter procedure we take into account an increase in energy by a factor of $f \sim 10$ due to refreshed shocks (Granot et al. 2003) between t_j and the times when the image size was measured. For simplicity, we do not include the effect of the energy injection on the early image size. The image size that is calculated in this way is not valid before the end of the energy injection episode (after several days), but it should be reasonably accurate at $t \gtrsim 25$ days, when its value is measured. The values of E/A and Γ(25 days) from these fits are indicated in Figure 6 and in Table 1.

For $a = (0.25,\ 0.5,\ 0.75)$ we obtain $\beta_{\rm ap} \approx (1.4,\ 2.8,\ 4.2)$, $\Gamma_* \approx (1.7,\ 3.0,\ 4.4)$, and $\Gamma(\theta_*) \approx (1.5,\ 2.4,\ 3.4)$. The values of $\Gamma(\theta_*)$ are similar to the values of Γ that were obtained from the fit to the observed image size for model 1 and model 2 with $k = 2$, but the value is smaller for model 1 with $k = 0$, as expected (see discussion at end of § 3).

Using the radio data from Berger et al. (2003), we find that $F_\nu \approx 10$ mJy at $t \approx 25$ days and $\nu = 4.86$ GHz, which according to the spectrum at this time is below $\nu_{\rm sa}$. Berger et al. (2003) also estimated the break frequencies at $t \approx 10$ days to be $\nu_{\rm sa} \approx 19$ GHz and $\nu_m \approx 43$ GHz, which is consistent with $\nu < \nu_{\rm sa} < \nu_m$ at $t = 24.5$ days. A value of $p = 2.25$ was inferred for GRB 030329 (Willingale et al. 2004). For the power-law segment of the spectrum, where $F_\nu \propto \nu^2$ (labeled "B" in Fig. 1 of Granot & Sari 2002), we have $\gamma_{\rm eff} \approx \gamma_m$, for which equations (1) and (3) imply

$$\epsilon_e \approx \frac{1}{2\pi}\left(\frac{p-1}{p-2}\right)\frac{(1+z)}{\Gamma(\Gamma-1)}\left(\frac{D_A}{R_\perp}\right)^2\frac{F_\nu}{m_p\nu^2}. \qquad (8)$$

[8] Throughout this paper we assume $\Omega_M = 0.27$, $\Omega_\Lambda = 0.73$, and $H_0 = 71$ km s^{-1} Mpc^{-1}.

[9] Applying the Bayesian inference formalism developed by Reichart et al. (2001), we determine values and uncertainties for the model parameter a. Bayesian inference formalism deals only with measurements with Gaussian error distributions, not with lower or upper limits. However, this formalism can be straightforwardly generalized to deal with limits as well, using two facts: (1) a limit can be given by the convolution of a Gaussian distribution and a Heaviside function, and (2) convolution is associative.

TABLE 1
COMPARING THE VALUES OF PHYSICAL PARAMETERS DERIVED FROM DIFFERENT OBSERVABLES

External Density	Physical Parameter	Observables Being Used	Model 1	Model 2	Major Source of Uncertainty	Uncertain by a Factor of
$k = 0$	E_{51}/n_0.....	F_ν(10 days)	$0.024\nu_{c,13}^{-3/8}$	$0.40\nu_{c,13}^{-3/8}$	$\propto \nu_{\rm sa}^{-15/4}\nu_m^{-15/8}F_{\nu,\max}^{9/4}$	~10–100
		$R_\perp(t)$	0.8	5	$\propto R_\perp^{6(3)}$ in model 1 (2)	~10 (~5)
$k = 2$	E_{51}/A_*	F_ν(10 days)	$0.31\nu_{c,13}^{-1/8}$	$0.10\nu_{c,13}^{-1/8}$	$\propto \nu_{\rm sa}^{-5/4}\nu_m^{-5/8}F_{\nu,\max}^{3/4}$	~2–3
		$R_\perp(t)$	2	1.2	$\propto R_\perp^{3(1)}$ in model 1 (2)	~5 (~2)
$k = 0$	Γ(25 days).....	$R_\perp$	2.4	1.5	$R_\perp$(obs) and $\Gamma(\theta_*)$	~1.3
		$R_\perp$	2.1	2.4	$R_\perp$(obs) and jet model	~1.1–1.2
$k = 2$	Γ(25 days).....	$R_\perp$	2.4	2.4	$R_\perp$(obs) and $\Gamma(\theta_*)$	~1.3
		$R_\perp$	2.6	2.8	$R_\perp$(obs) and jet model	~1.1–1.2
$k = 0$	ϵ_e.....	$R_\perp$, $F_{\nu<\nu_{\rm sa}}$	0.023	0.10	$R_\perp$ and $\Gamma(\theta_*)$ in eq. (8)	~10
		$R_\perp$, $F_{\nu<\nu_{\rm sa}}$	0.035	0.024	$R_\perp$ and Γ(Fig. 6) in eq. (8)	~5–10
		F_ν(10 days)	$0.24\nu_{c,13}^{1/4}$	$0.078\nu_{c,13}^{1/4}$	Model and value of ν_c	~3
$k = 2$	ϵ_e.....	$R_\perp$, $F_{\nu<\nu_{\rm sa}}$	0.023	0.023	$R_\perp$ and $\Gamma(\theta_*)$ in eq. (8)	~10
		$R_\perp$, $F_{\nu<\nu_{\rm sa}}$	0.020	0.017	$R_\perp$ and Γ(Fig. 6) in eq. (8)	~5–10
		F_ν(10 days)	$0.36\nu_{c,13}^{1/4}$	$0.17\nu_{c,13}^{1/4}$	Model and value of ν_c	~3

NOTES.—Estimates for the physical parameters of GRB 030329 derived from different observable quantities for different models of the jet lateral expansion. The value of E/A is estimated from the spectrum at 10 days (first line) and from the fit to the observed image size (second line). The value of Γ(25 days) is evaluated both as $\Gamma(\theta_*)$ according to § 2 (first line) and from the fit to the observed image size (second line). The value of ϵ_e in the first two lines is evaluated using eq. (8) with the values of Γ(25 days) from the corresponding lines. In the third line the value of ϵ_e is from the spectrum at 10 days.

Using the above values for the flux, $R_\perp$, $\Gamma(\theta_*)$, and p for GRB 030329, equation (8) gives $\epsilon_e \approx (0.10,\ 0.023,\ 0.0099)$ for $a = (0.25,\ 0.5,\ 0.75)$. These values of ϵ_e are somewhat on the low side compared to the values inferred from broadband afterglow modeling of other afterglows (e.g., Panaitescu & Kumar 2001). In Table 1 we show, in addition to these values of ϵ_e, the values that are obtained when evaluating Γ from the fit to the image size that is shown in Figure 6. The largest difference between these two estimates of ϵ_e is for model 1 with $k = 0$, for which evaluating Γ from the fit to the observed source size probably provides a more accurate estimate.

Since equation (8) relies on a small number of assumptions, it is rather robust. However, the value of ϵ_e in equation (8) is very sensitive to the value of $R_\perp$. This is because $\epsilon_e \propto 1/R_\perp^2\Gamma(\Gamma-1)$, and for $\Gamma \gg 1$ we have $\Gamma \approx \Gamma_*/\sqrt{2} \approx \beta_{\rm ap}/\sqrt{2} = a\langle\beta_{\rm ap}\rangle/\sqrt{2} \propto R_\perp$, so that $\epsilon_e \propto R_\perp^{-4}$. For example, $\theta_s = 45$ μas ($R_\perp = 0.064$ pc) at $t = 24.5$ days, which is still within the measurement errors, would imply $\epsilon_e = (0.61,\ 0.14,\ 0.060)$ for $a = (0.25,\ 0.5,\ 0.75)$. The latter values, especially for $a \approx 0.5$, are consistent with the value found by Willingale et al. (2004) from a broadband fit to the afterglow data, $\epsilon_e = 0.24$ and $0.18 < \epsilon_e < 0.31$ at the 90% confidence level, and with the value of $\epsilon_e \approx 0.16$ found by Berger et al. (2003).

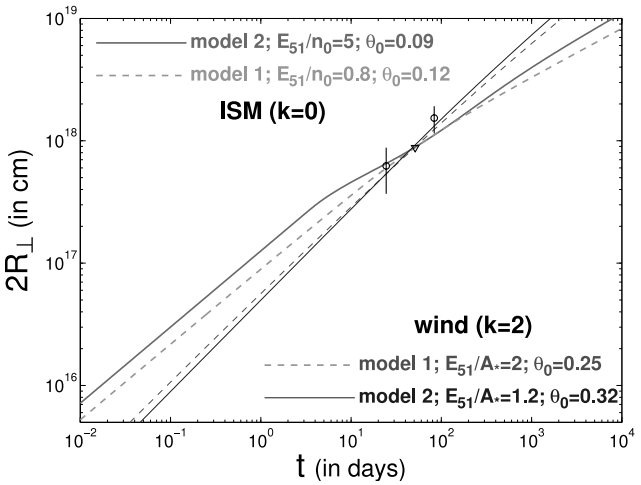

FIG. 6.—Tentative fit of a simple semianalytic realization of models 1 and 2 to the observed image size (of diameter $2R_\perp$). The physical parameters and external density profile for each model are indicated. [*See the electronic edition of the Journal for a color version of this figure.*]

7. INFERRING THE PHYSICAL PARAMETERS FROM A SNAPSHOT SPECTRUM AT $t_j < t < t_{\rm NR}$

For model 1, we obtain expressions for the peak flux and break frequencies at $t_j < t < t_{\rm NR}$ by using the expressions for $t < t_j$ from Granot & Sari (2002) in order to estimate their values at t_j, and then using their temporal scalings at $t_j < t < t_{\rm NR}$ from Rhoads (1999) and Sari et al. (1999). In Appendix C we provide expressions for the peak flux and break frequencies as a function of the physical parameters and solve them for the physical parameter as a function of the peak flux and break frequencies for both models 1 and 2. The results for GRB 030329 are given below.

For GRB 030329, Berger et al. (2003) infer $\nu_{\rm sa} \approx 19$ GHz, $\nu_m \approx 43$ GHz, and $F_{\nu,\max} \approx 96$ mJy at $t \approx 10$ days, as well as $p = 2.2$. Using equations (4.13)–(4.16) of Sari & Esin (2001), Berger et al. (2003) find $E_{\rm iso,52} \approx 0.56\nu_{c,13}^{1/4}$, $n_0 \approx 1.8\nu_{c,13}^{3/4}$, $\epsilon_B \approx 0.10\nu_{c,13}^{-5/4}$, and $\epsilon_e \approx 0.16\nu_{c,13}^{1/4}$, and using a value of $\theta_j \approx 0.3$ at this time they infer $E_{51} \approx 0.25$. For the same values of the spectral parameters and using our model 1, we obtain $E_{\rm iso,52} = 0.16\nu_{c,13}^{1/4}$, $E_{51} = 0.36\nu_{c,13}^{3/8}$, $n_0 = 15\nu_{c,13}^{3/4}$, $\epsilon_B = 0.12\nu_{c,13}^{-5/4}$, and $\epsilon_e = 0.24\nu_{c,13}^{1/4}$ for $k = 0$, and $E_{\rm iso,52} = 0.10\nu_{c,13}^{1/4}$, $E_{51} = 0.43\nu_{c,13}^{3/8}$, $A_* = 1.4\nu_{c,13}^{1/2}$, $\epsilon_B = 0.034\nu_{c,13}^{-5/4}$, and $\epsilon_e = 0.36\nu_{c,13}^{1/4}$ for $k = 2$. The implied values of E/A are shown in Table 1. The differences between our values and those of Berger et al. (2003) arise from differences by factors of order unity between the coefficients in the expressions for the peak flux and break frequencies. This typically results in differences by factors of order unity in the inferred values of the physical parameters. The difference in the external density n is relatively large since it contains high powers of $\nu_{\rm sa}$ and ν_m (Granot et al. 1999b), making it more sensitive to the exact theoretical expressions and observational values of these frequencies.

For model 1 and $k = 0$ we obtain $E_{51}/n_0 = 0.0.024\nu_{c,13}^{-3/8}$, compared to $E_{51}/n_0 = 0.14\nu_{c,13}^{-1/2}$ from Berger et al. (2003) and $E_{51}/n_0 \sim 0.8$ that we obtain from the fit to the observed image size (Fig. 6). Because of the large uncertainty in the value of n

that is determined from the snapshot spectrum, and because of the large uncertainty in the value of E/n from the fit to the image size, these values are consistent with each other within their reasonable errors (see Table 1). For model 1 and $k = 2$ we obtain $E_{51}/A_* = 0.31\nu_{c,13}^{-1/8}$, compared to $E_{51}/A_* \approx 0.8$ from the fit to the observed image size. Here the difference between the two values is smaller, but the uncertainty on the two values is also smaller (see Table 1). Altogether, the two values are still consistent within their estimated errors.

For our model 2 involving a jet with no significant lateral spreading, the peak flux is suppressed by a factor of $(t/t_j)^{-(3-k)/(4-k)}$, where $t_j \approx 0.5$ days and $t/t_j \approx 20$, i.e., a factor of $\approx$0.11 for $k = 0$ and $\approx$0.22 for $k = 2$. This implies (see Appendix C) $E_{\rm iso,52} = 4.7\nu_{c,13}^{1/4}$, $E_{51} = 0.21\nu_{c,13}^{3/8}$, $n_0 = 0.53\nu_{c,13}^{3/4}$, $\epsilon_B = 0.37\nu_{c,13}^{-5/4}$, and $\epsilon_e = 0.078\nu_{c,13}^{1/4}$ for $k = 0$, and $E_{\rm iso,52} = 0.98\nu_{c,13}^{1/4}$, $E_{51} = 0.29\nu_{c,13}^{3/8}$, $A_* = 1.4\nu_{c,13}^{1/2}$, $\epsilon_B = 0.071\nu_{c,13}^{-5/4}$, and $\epsilon_e = 0.17\nu_{c,13}^{1/4}$ for $k = 2$. For model 2 with $k = 0$ we get $E_{51}/n_0 = 0.40\nu_{c,13}^{-3/8}$, compared to $E_{51}/n_0 \approx 5$ from the fit to the observed image size. These two values are consistent within the large uncertainties on both values (see Table 1).

For model 2 with $k = 2$ we obtain $E_{51}/A_* = 0.10\nu_{c,13}^{-1/8}$, compared to $E_{51}/A_* \approx 1.2$ from the fit to the observed image size. In this case, however, the errors on these two values are relatively small (see Table 1). This is because (1) the image size is linear in E/A, which corresponds to a relatively strong dependence, and therefore the observed image size can constrain the value of E/A relatively well, and (2) the expression for E/A from the spectrum contains relatively small powers of the break frequencies and peak flux and thus has a correspondingly small uncertainty. Therefore, the two values of E_{51}/A_* are farther apart than is expected from the uncertainty on these values. Thus, one might say that the data disfavor model 2 with $k = 2$. It is difficult, however, to rule out this model altogether, because of the uncertainty in the exact expressions for the break frequencies and peak flux at $t_j < t < t_{\rm NR}$.

8. DISCUSSION

We have analyzed the data on the time-dependent image size of the radio afterglow of GRB 030329 (Taylor et al. 2004) and constrained the physical parameters of this explosion. The image size was measured after the jet break time t_j in the afterglow light curve, where existing theoretical models still have a high level of uncertainty regarding the jet dynamics. This motivated us to consider two extreme models of the lateral expansion of the jet: model 1, where there is relativistic lateral expansion in the local rest frame of the jet at $t_j < t < t_{\rm NR}$, and model 2, with no significant lateral expansion until the transition time to a nonrelativistic expansion $t_{\rm NR}$. We have tested the predictions of these models against the observations, for both a uniform ($\rho_{\rm ext} = Ar^{-k}$, with $k = 0$) and a stellar wind ($k = 2$) external density profile.

The observational constraints included comparisons between (1) the value of the postshock energy fraction in relativistic electrons ϵ_e that is inferred from the source size and flux below the self-absorption frequency and its value from the snapshot spectrum at $t \approx 10$ days, (2) the value of E/A that is inferred from the source size and its value from the snapshot spectrum at $t \approx 10$ days, and (3) the observed temporal evolution of the source size and the theoretical predictions. We have found that most models pass all these tests. The only exception is model 2 with $k = 2$, involving a relativistic jet with little lateral expansion (well before $t_{\rm NR}$) that is propagating in a stellar wind external medium, which does poorly on constraint 3 above.

We have found that for a jet with little lateral expansion before $t_{\rm NR}$ (our model 2), the jet would become roughly spherical only long after $t_{\rm NR}$ (see eq. [6] and the discussion around it). This introduces a fast growth in the image size near $t_{\rm NR}$ for on-axis observers with $\theta_{\rm obs} < \theta_0$ (see Fig. 3, *top*) that detects the prompt gamma-ray emission (as in the case of GRB 030329). For an observer at $\theta_{\rm obs} \approx 90^\circ$, as would typically be the case for GRBs that might be found in nearby Type Ib/c supernovae months to years after the supernova explosion (Paczyński 2001; Granot & Loeb 2003; Ramirez-Ruiz & Madau 2004), this causes a very slow increase in the image size near $t_{\rm NR}$ (see Fig. 3, *bottom*).

Our conclusions differ from those of Oren et al. (2004), who argue that model 2 with $k = 0$ is the only model that can be ruled out, while the other models are consistent with the data. We find that model 2 with $k = 0$ is consistent with the data (as well as model 1), while model 2 with $k = 2$ is disfavored by the data. The different conclusion regarding model 2 with $k = 0$ arises since we choose a value of E/n that gives the observed image size at 25 days, instead of the value from the snapshot spectrum that was used by Oren et al. (2004), and since we allow for some lateral spreading around $t_{\rm NR}$, which is expected physically, while they assumed zero lateral expansion. The latter provides a good fit to the observed source size at 83 days and is consistent with the upper limit at 53 days. The different conclusion regarding model 2 with $k = 2$ arises since Oren et al. (2004) did not address constraint 2.

The formalism developed in this paper would be useful for the analysis of future radio imaging of nearby GRB afterglows. The forthcoming *Swift* satellite[10] is likely to discover new GRBs at low redshifts. Follow-up imaging of their radio jets will constrain their physical properties and reveal whether the conclusions that we derived for GRB 030329 apply more generally to other relativistic explosions.

We thank Tsvi Piran, Yonatan Oren, and Ehud Nakar for useful discussions that helped improve the paper. This work was supported by the W. M. Keck foundation and NSF grant PHY 00-70928 (J. G.), and by NASA through Chandra Postdoctoral Fellowship award PF3-40028 (E. R.-R.). It was also supported in part by NASA grant NAG5-13292 and by NSF grants AST 00-71019 and AST 02-04514 (A. L.).

[10] See http://swift.gsfc.nasa.gov.

APPENDIX A

THE ANGLE θ_* ON THE EQUAL ARRIVAL TIME SURFACE WHERE $R_\perp$ IS LOCATED

The time at which a photon emitted at a lab-frame time $t_{\rm lab}$ and at spherical coordinates (r, θ, ϕ) reaches the observer is given by

$$t = t_{\rm lab} - (R/c)\cos\theta \tag{A1}$$

and is referred to as the observed time, where for convenience the direction to the observer is chosen to be along the z-axis (i.e., at $\theta = 0$). Let the location of a spherically symmetric shock front (or any other emitting surface for that matter) be described by $r = R(t_{\rm lab})$, and that of an axially symmetric shock front by $r = R(t_{\rm lab}, \theta)$. We now calculate the angle θ_* on the equal arrival time surface (which is defined by $t = {\rm const}$) where $R_\perp = \max(R \sin\theta)$ is located. At this point on the equal arrival time surface we have

$$0 = \left(\frac{\partial R \sin\theta}{\partial\theta}\right)_t = \left(\frac{\partial R \sin\theta}{\partial\theta}\right)_{t_{\rm lab}} + \left(\frac{\partial R \sin\theta}{\partial t_{\rm lab}}\right)_\theta \left(\frac{\partial t_{\rm lab}}{\partial\theta}\right)_t = R(\cos\theta + \tilde{R}_\theta \sin\theta) + \beta_r c \sin\theta \left(\frac{\partial t_{\rm lab}}{\partial\theta}\right)_t, \tag{A2}$$

where we use the notions $(\partial R/\partial t_{\rm lab})_\theta = \beta_r c$ and $\tilde{R}_\theta = (\partial \ln R/\partial\theta)_{t_{\rm lab}}$. From equation (A1) we have

$$0 = \left(\frac{\partial t}{\partial\theta}\right)_t = \frac{R}{c}(\sin\theta - \tilde{R}_\theta \cos\theta) + (1 - \beta_r \cos\theta)\left(\frac{\partial t_{\rm lab}}{\partial\theta}\right)_t, \tag{A3}$$

so that

$$\left(\frac{\partial t_{\rm lab}}{\partial\theta}\right)_t = \frac{R}{c}\left(\frac{\tilde{R}_\theta \cos\theta - \sin\theta}{1 - \beta_r \cos\theta}\right). \tag{A4}$$

Substituting equation (A4) into equation (A2) we obtain

$$\cos\theta = \beta_r - \tilde{R}_\theta \sin\theta = \frac{1}{c}\left(\frac{\partial R}{\partial t_{\rm lab}}\right)_\theta - \frac{\sin\theta}{R}\left(\frac{\partial R}{\partial\theta}\right)_{t_{\rm lab}}. \tag{A5}$$

For a spherically symmetric shock $\tilde{R}_\theta = 0$ and $\cos\theta_* = \beta_r(\theta_*) = \beta_*$, where in this case β_r is the shock velocity at the point on the equal arrival time surface where $\theta = \theta_*$ and $R_\perp$ is located. For a shock with axial symmetry we have

$$\cos\theta_* = \frac{\beta_r - \tilde{R}_\theta\sqrt{1 - \beta_r^2 + \tilde{R}_\theta^2}}{1 + \tilde{R}_\theta^2}, \tag{A6}$$

$$\beta_r = \beta_*\sqrt{1 + \tilde{R}_\theta^2}, \tag{A7}$$

where β_* is the shock velocity component normal to the shock front in the rest frame of the upstream medium, which is the one that enters into the shock jump conditions (Kumar & Granot 2003).

APPENDIX B

THE APPARENT VELOCITY

The apparent velocity, $\beta_{\rm ap} = [(1+z)/c](dR_\perp/dt)$, for a point source moving with a velocity β at an angle θ from our line of sight is

$$\beta_{\rm ap} = \frac{\beta\sin\theta}{1 - \beta\cos\theta}. \tag{B1}$$

For a spherical shock front moving at a constant velocity $\beta_{\rm sh}$, $R_\perp$ is located at a constant angle θ_* that satisfies $\cos\theta_* = \beta_* = \beta_{\rm sh} = {\rm const}$ (according to eq. [A5]), so that the apparent velocity of the edge of the observed image is simply given by substituting $\cos\theta_* = \beta_*$ in equation (B1). This gives

$$\beta_{\rm ap} = \Gamma_*\beta_* = \sqrt{\Gamma_*^2 - 1}. \tag{B2}$$

We now show that this result holds for any spherically symmetric shock front. At $t + dt$ we have

$$\theta_*(t + dt) = \theta_*(t) + d\theta_*, \qquad \beta_*(t + dt) = \beta_*(t) + d\beta_*, \qquad d\beta_* = d\cos\theta_* \propto dt, \tag{B3}$$

and since equation (B2) holds for a sphere moving at a constant velocity, we have

$$(R\sin\theta)(t + dt,\ \theta_*) = R_\perp(t) + \Gamma_*(t)\beta_*(t)c\,dt + O(dt^2). \tag{B4}$$

Now, since $R_\perp$ is located where $(\partial R\sin\theta/\partial\theta)_t = 0$, then

$$R_\perp(t + dt) = (R\sin\theta)(t + dt,\ \theta_* + d\theta_*) = (R\sin\theta)(t + dt,\ \theta_*) + O(dt^2) = R_\perp(t) + \Gamma_*(t)\beta_*(t)c\,dt + O(dt^2), \tag{B5}$$

and therefore equation (B2) holds for any spherically symmetric shock front.

Finally, for an axially symmetric shock front, we obtain, based on considerations similar to those in the spherical case,

$$\beta_{\rm ap} = \frac{\beta_r \sin\theta_*}{1 - \beta_r \cos\theta_*}, \tag{B6}$$

where θ_* and β_r are given by equations (A6) and (A7), respectively.

APPENDIX C

SOLVING FOR THE PHYSICAL PARAMETERS FROM A SNAPSHOT SPECTRUM AT $t > t_j$

The most common ordering of the spectral break frequencies at $t_j < t < t_{\rm NR}$ is $\nu_{\rm sa} < \nu_m < \nu_c$, for which we obtain

$$\nu_{\rm sa} = 2.08\times10^{9}\frac{(p-1)^{8/5}}{(p-2)(3p+2)^{3/5}}(1+z)^{-4/5}\epsilon_e^{-1}\epsilon_B^{1/5}n_0^{8/15}E_{51}^{4/15}t_{\rm days}^{-1/5}\ {\rm Hz}, \tag{C1}$$

$$\nu_m = 1.35\times10^{16}\left(\frac{p-2}{p-1}\right)^2(p-0.67)(1+z)\epsilon_e^{2}\epsilon_B^{1/2}n_0^{-1/6}E_{51}^{2/3}t_{\rm days}^{-2}\ {\rm Hz}, \tag{C2}$$

$$\nu_c = 1.75\times10^{13}(p-0.46)e^{-1.16p}(1+z)^{-1}\epsilon_B^{-3/2}n_0^{-5/6}E_{51}^{-2/3}(1+Y)^{-2}\ {\rm Hz}, \tag{C3}$$

$$F_{\nu,\rm max} = 131(p+0.14)(1+z)^2\epsilon_B^{1/2}n_0^{1/6}E_{51}^{4/3}t_{\rm days}^{-1}D_{L,28}^{-2}\ {\rm mJy} \tag{C4}$$

for a uniform external medium ($k = 0$), and

$$\nu_{\rm sa} = 3.85\times10^{9}\frac{(p-1)^{8/5}}{(p-2)(3p+2)^{3/5}}(1+z)^{-4/5}\epsilon_e^{-1}\epsilon_B^{1/5}A_*^{8/5}E_{51}^{-4/5}t_{\rm days}^{-1/5}\ {\rm Hz}, \tag{C5}$$

$$\nu_m = 1.05\times10^{16}\left(\frac{p-2}{p-1}\right)^2(p-0.69)(1+z)\epsilon_e^{2}\epsilon_B^{1/2}A_*^{-1/2}E_{51}t_{\rm days}^{-2}\ {\rm Hz}, \tag{C6}$$

$$\nu_c = 1.15\times10^{11}(3.45-p)e^{0.45p}(1+z)^{-1}\epsilon_B^{-3/2}A_*^{-5/2}E_{51}(1+Y)^{-2}\ {\rm Hz}, \tag{C7}$$

$$F_{\nu,\rm max} = 201(p+0.12)(1+z)^2\epsilon_B^{1/2}A_*^{1/2}E_{51}t_{\rm days}^{-1}D_{L,28}^{-2}\ {\rm mJy} \tag{C8}$$

for a stellar wind environment ($k = 2$), where Y is the Compton y-parameter, $A_* = A/(5\times10^{11}\ {\rm g\ cm^{-1}})$, $t_{\rm days} = t/(1\ {\rm day})$, ϵ_B is the fraction of the internal energy behind the shock in the magnetic field, and $Q_x \equiv Q/(10^x \times$ the cgs units of Q). The emission depends only on the true energy in the jet, E, and does not depend on its initial half-opening angle θ_0, since at $t > t_j$ (or equivalently when Γ drops below θ_0^{-1}), the dynamics become independent of θ_0; i.e., the jet begins to expand sideways exponentially with radius in a self-similar manner that is independent of θ_0 (Granot et al. 2002). Solving the above sets of equations for the physical parameters yields

$$E_{\rm iso,52} = 0.104\frac{f_0(p)}{f_0(2.2)}\nu_{a,9}^{-5/6}\nu_{m,13}^{-5/12}\nu_{c,14}^{1/4}\left(\frac{F_{\nu,\rm max}}{1\ {\rm mJy}}\right)^{3/2}t_{\rm days}^{-1/2}(1+z)^{-2}D_{L,28}^{3}(1+Y)^{1/2}, \tag{C9}$$

$$E_{51} = 0.0136\frac{g_{0,E}(p)}{g_{0,E}(2.2)}\nu_{a,9}^{5/12}\nu_{m,13}^{5/24}\nu_{c,14}^{3/8}\left(\frac{F_{\nu,\rm max}}{1\ {\rm mJy}}\right)^{3/4}t_{\rm days}^{5/4}(1+z)^{-1}D_{L,28}^{3/2}(1+Y)^{3/4}, \tag{C10}$$

$$n_0 = 0.0714\frac{g_n(p)}{g_n(2.2)}\nu_{a,9}^{25/6}\nu_{m,13}^{25/12}\nu_{c,14}^{3/4}\left(\frac{F_{\nu,\rm max}}{1\ {\rm mJy}}\right)^{-3/2}t_{\rm days}^{7/2}(1+z)^{5}D_{L,28}^{-3}(1+Y)^{3/2}, \tag{C11}$$

$$\epsilon_B = 2.42\frac{g_{0,B}(p)}{g_{0,B}(2.2)}\nu_{a,9}^{-5/2}\nu_{m,13}^{-5/4}\nu_{c,14}^{-5/4}\left(\frac{F_{\nu,\rm max}}{1\ {\rm mJy}}\right)^{1/2}t_{\rm days}^{-5/2}(1+z)^{-3}D_{L,28}(1+Y)^{-5/2}, \tag{C12}$$

$$\epsilon_e = 0.355\frac{g_{0,e}(p)}{g_{0,e}(2.2)}\nu_{a,9}^{5/6}\nu_{m,13}^{11/12}\nu_{c,14}^{1/4}\left(\frac{F_{\nu,\rm max}}{1\ {\rm mJy}}\right)^{-1/2}t_{\rm days}^{3/2}(1+z)D_{L,28}^{-1}(1+Y)^{1/2} \tag{C13}$$

for a uniform density, where $f_0(p) = e^{0.29p}(p-1)^{1/2}(3p+2)^{-1/2}(p-0.67)^{5/12}(p-0.46)^{-1/4}(p+0.14)^{-3/2}$, $g_{0,E}(p) = e^{0.435p}(p-1)^{-1/4}(3p+2)^{1/4}(p-0.67)^{-5/24}(p-0.46)^{-3/8}(p+0.14)^{-3/4}$, $g_n(p) = e^{0.87p}(p-1)^{-5/2}(3p+2)^{5/2}(p-0.67)^{-25/12}(p-0.46)^{-3/4}(p+0.14)^{3/2}$, $g_{0,B}(p) = e^{-1.45p}(p-1)^{3/2}(3p+2)^{-3/2}(p-0.67)^{5/4}(p-0.46)^{5/4}(p+0.14)^{-1/2}$, and $g_{0,e}(p) = e^{0.29p}(p-2)^{-1}(p-1)^{1/2}(3p+2)^{1/2}(p-0.67)^{-11/12}(p-0.46)^{-1/4}(p+0.14)^{1/2}$. For a stellar wind environment we find

$$E_{\rm iso,52} = 0.0674\frac{f_2(p)}{f_2(2.2)}\nu_{a,9}^{-5/6}\nu_{m,13}^{-5/12}\nu_{c,14}^{1/4}\left(\frac{F_{\nu,\rm max}}{1\ {\rm mJy}}\right)^{3/2}t_{\rm days}^{-1/2}(1+z)^{-2}D_{L,28}^{3}(1+Y)^{1/2}, \tag{C14}$$

$$E_{51} = 0.0161 \frac{g_{2,E}(p)}{g_{2,E}(2.2)} \nu_{a,9}^{5/12} \nu_{m,13}^{5/24} \nu_{c,14}^{3/8} \left(\frac{F_{\nu,\max}}{1\ \mathrm{mJy}}\right)^{3/4} t_{\mathrm{days}}^{5/4} (1+z)^{-1} D_{L,28}^{3/2} (1+Y)^{3/4}, \tag{C15}$$

$$A_* = 0.0262 \frac{g_A(p)}{g_A(2.2)} \nu_{a,9}^{5/3} \nu_{m,13}^{5/6} \nu_{c,14}^{1/2} t_{\mathrm{days}}^2 (1+z)(1+Y), \tag{C16}$$

$$\epsilon_B = 0.680 \frac{g_{2,B}(p)}{g_{2,B}(2.2)} \nu_{a,9}^{-5/2} \nu_{m,13}^{-5/4} \nu_{c,14}^{-5/4} \left(\frac{F_{\nu,\max}}{1\ \mathrm{mJy}}\right)^{1/2} t_{\mathrm{days}}^{-5/2} (1+z)^{-3} D_{L,28} (1+Y)^{-5/2}, \tag{C17}$$

$$\epsilon_e = 0.526 \frac{g_{2,e}(p)}{g_{2,e}(2.2)} \nu_{a,9}^{5/6} \nu_{m,13}^{11/12} \nu_{c,14}^{1/4} \left(\frac{F_{\nu,\max}}{1\ \mathrm{mJy}}\right)^{-1/2} t_{\mathrm{days}}^{3/2} (1+z) D_{L,28}^{-1} (1+Y)^{1/2}, \tag{C18}$$

where $f_2(p) = e^{-0.113p}(p-1)^{1/2}(3p+2)^{-1/2}(p-0.69)^{5/12}(3.45-p)^{-1/4}(p+0.12)^{-3/2}$, $g_{2,E}(p) = e^{-0.169p}(p-1)^{-1/4}(3p+2)^{1/4}(p-0.69)^{5/4}(3.45-p)^{5/4}(p+0.12)^{3/4}$, $g_A(p) = e^{-0.225p}(p-1)^{-1}(3p+2)(p-0.69)^{-5/6}(3.45-p)^{-1/2}$, $g_{2,B}(p) = e^{0.563p}(p-1)^{3/2}(3p+2)^{-3/2}(p-0.69)^{5/4}(3.45-p)^{5/4}(p+0.12)^{-1/2}$, and $g_{2,e}(p) = e^{-0.113p}(p-2)^{-1}(p-1)^{1/2}(3p+2)^{1/2}(p-0.69)^{-11/12}(3.45-p)^{-1/4}(p+0.12)^{1/2}$.

As was pointed out by Sari & Esin (2001), the expressions for the physical parameters that are derived from the instantaneous ("snapshot") spectrum do not depend on the external density profile (i.e., on the value of k in our case), up to factors of order unity. This is because the instantaneous spectrum samples only the instantaneous external density just in front of the afterglow shock, $n_{\mathrm{ext}}(r)$. The expression for the external density n for a uniform medium ($k = 0$) represents the density just in front of the shock for a general density profile that varies smoothly and gradually with radius, $n \leftrightarrow n_{\mathrm{ext}}(r)$, where in our case $n_{\mathrm{ext}} = Ar^{-k}/m_p$. However, for a nonuniform density n_{ext} changes with radius and therefore with time. In our case, we assume that the functional form of $n_{\mathrm{ext}}(r)$ is known (i.e., we fix the value of k) and express the density normalization A as a function of the instantaneous values of the peak flux and break frequencies.

We note that the expressions for the physical parameters at $t_j < t < t_{\mathrm{NR}}$ are identical to those at $t < t_j$. This is because we assume that the jet is uniform within a half-opening angle $\theta_j \approx \Gamma^{-1}$ and therefore that its emission is practically indistinguishable from that of a spherical blast wave with the same Lorentz factor Γ and radius R, or equivalently,[11] the same isotropic equivalent energy E_{iso} [which for a spherical blast wave is equal to the true energy, and for a model 1 jet is $E_{\mathrm{iso}} \approx (2/\theta_j^2)E \approx 2\Gamma^2 E$] and observed time t (for the same values of n_{ext}, ϵ_e, ϵ_B, and p).

At $t < t_j$, $E_{\mathrm{iso}} = \mathrm{const}$ and is the more interesting physical quantity, while E in equations (C10) and (C15) represents the energy within an angle of Γ^{-1} around our line of sight, which has no special physical significance at this stage. At $t_j < t < t_{\mathrm{NR}}$, however, the situation is reversed and $E = \mathrm{const}$ represents the true kinetic energy of the jet and is therefore of great interest, while $E_{\mathrm{iso}} \approx 2\Gamma^2 E$ decreases with time and is no longer a very interesting physical quantity.

For model 2, the jet continues to evolve as if it were part of a spherical blast wave with the same E_{iso} until $t_{\mathrm{NR}}(E_{\mathrm{iso}})$, and $E_{\mathrm{iso}} \approx (2/\theta_0^2)E = \mathrm{const}$. Therefore, the emission at $t_j < t < t_{\mathrm{NR}}$ is the same as from a spherical blast wave with the same E_{iso}, except for the peak flux $F_{\nu,\max}$, which is suppressed by a factor of $\sim(\theta_0\Gamma)^2 \approx (t/t_j)^{-(3-k)/(4-k)}$. Hence, the above equations for the physical parameters can still be used in this case with the substitution $F_{\nu,\max} \rightarrow F_{\nu,\max}(t/t_j)^{(3-k)/(4-k)}$. In addition to this, in order to obtain the true energy in the jet, the expression for E (eqs. [C10] and [C15]) should be multiplied by $(t/t_j)^{-(3-k)/(4-k)}$, which is the fraction of the area within an angle of Γ^{-1} around the line of sight that is occupied by the jet.

[11] This is since Γ and R are functions of E_{iso}, $n_{\mathrm{ext}} = \rho_{\mathrm{ext}}/m_p$ and t: $E_{\mathrm{iso}} \sim \Gamma^2 R^2 \rho_{\mathrm{ext}} c^2$ and $t \sim R/c\Gamma^2$ so that $R \sim (E_{\mathrm{iso}} t/\rho_{\mathrm{ext}} c)^{1/4}$ and $\Gamma \sim (E_{\mathrm{iso}}/\rho_{\mathrm{ext}} c^5 t^3)^{1/8}$.

REFERENCES

Ayal, S., & Piran, T. 2001, ApJ, 555, 23
Begelman, M. C., Blandford, R. D., & Rees, M. J. 1984, Rev. Mod. Phys., 56, 255
Berger, E., et al. 2003, Nature, 426, 154
Blandford, R. D., & McKee, C. F. 1976, Phys. Fluids, 19, 1130
Cannizzo, J. K., Gehrels, N., & Vishniac, E. T. 2004, ApJ, 601, 380
Cen, R. 1999, ApJ, 524, L51
Frail, D. A., Kulkarni, S. R., Nicastro, S. R., Feroci, M., & Taylor, G. B. 1997, Nature, 389, 261
Garnavich, P. M., Loeb, A., & Stanek, K. Z. 2000, ApJ, 544, L11
Gaudi, B. S., Granot, J., & Loeb, A. 2001, ApJ, 561, 178
Gaudi, B. S., & Loeb, A. 2001, ApJ, 558, 643
Ghisellini, G., & Lazzati, D. 1999, MNRAS, 309, L7
Goodman, J. 1997, NewA, 2, 449
Granot, J., & Königl, A. 2003, ApJ, 594, L83
Granot, J., & Loeb, A. 2001, ApJ, 551, L63
———. 2003, ApJ, 593, L81
Granot, J., Miller, M., Piran, T., Suen, W. M., & Hughes, P. A. 2001, in Gamma-Ray Bursts in the Afterglow Era, ed. E. Costa, F. Frontera, & J. Hjorth (Berlin: Springer), 312
Granot, J., Nakar, E., & Piran, T. 2003, Nature, 426, 138
Granot, J., Panaitescu, A., Kumar, P., & Woosley, S. E. 2002, ApJ, 570, L61
Granot, J., Piran, T., & Sari, R. 1999a, ApJ, 513, 679
———. 1999b, ApJ, 527, 236
Granot, J., Piran, T., & Sari, R. 2000, ApJ, 534, L163
Granot, J., & Ramirez-Ruiz, E. 2004, ApJ, 609, L9
Granot, J., & Sari, R. 2002, ApJ, 568, 820
Ioka, K., & Nakamura, T. 2001, ApJ, 561, 703
Katz, J. I., & Piran, T. 1997, ApJ, 490, 772
Kumar, P., & Granot, J. 2003, ApJ, 591, 1075
Loeb, A., & Perna, R. 1998, ApJ, 495, 597
Mao, S., & Loeb, A. 2001, ApJ, 547, L97
Medvedev, M., & Loeb, A. 1999, ApJ, 526, 697
Mirabel, I. F., & Rodríguez, L. F. 1999, ARA&A, 37, 409
Oren, Y., Nakar, E., & Piran, T. 2004, MNRAS, 353, L35
Paczyński, B. 2001, Acta Astron., 51, 1
Panaitescu, A., & Kumar, P. 2001, ApJ, 560, L49
Panaitescu, A., & Mészáros, P. 1998, ApJ, 493, L31
Ramirez-Ruiz, E., & Madau, P. 2004, ApJ, 608, L89
Reichart, D. E., Lamb, D. Q., Fenimore, E. E., Ramirez-Ruiz, E., Cline, T. L., & Hurley, K. 2001, ApJ, 552, 57
Rhoads, J. E. 1999, ApJ, 525, 737
Rossi, E. M., Lazzati, D., Salmonson, J. D., & Ghisellini, G. 2004, MNRAS, submitted (astro-ph/0401124)
Sagiv, A., Waxman, E., & Loeb, A. 2004, ApJ, 615, 366
Salmonson, J. D. 2003, ApJ, 592, 1002
Sari, R. 1998, ApJ, 494, L49
———. 1999, ApJ, 524, L43

Sari, R., & Esin, A. A. 2001, ApJ, 548, 787
Sari, R., Piran, T., & Halpern, J. P. 1999, ApJ, 519, L17
Sari, R., Piran, T., & Narayan, R. 1998, ApJ, 497, L17
Taylor, G. B., Frail, D. A., Berger, E., & Kulkarni, S. R. 2004, ApJ, 609, L1
Wang, X., & Loeb, A. 2001, ApJ, 552, 49
Waxman, E. 1997, ApJ, 491, L19
Waxman, E., Kulkarni, S. R., & Frail, D. A. 1998, ApJ, 497, 288
Willingale, R., et al. 2004, MNRAS, 349, 31
Woods, E., & Loeb, A. 1999, preprint (astro-ph/9907110)